

ARTICLE TYPE

Explicit dynamics of shells with a Flat-Facet Triangular Finite Element

Petr Krysl*

¹Structural Engineering Department,
University of California, San Diego,
California, USA

Correspondence

*Petr Krysl. Email: pkrysl@ucsd.edu

Summary

The use of a flat-facet finite element with three nodes and six degrees of freedom per node for modeling of linear wave-propagation events is discussed. The triangular shell finite element was presented in a preceding publication. The main novelty of the current approach is the treatment of the drilling rotations that decouples the drilling degree of freedoms on the global level, and hence makes it possible to eliminate negative effects of these degrees of freedom on the explicit time-stepping algorithms employed to compute the dynamic response, such as deterioration in accuracy or artificially reduced time step. The element is shown to be robust for wave propagation simulations, and its performance is illustrated with examples including guided-wave scenarios.

KEYWORDS:

flat facet shell finite element, discrete shear gap, drilling rotation, branched shells, folded shells

INTRODUCTION

Structures modeled as shells are commonly employed in the civil and marine engineering, aerospace, aeronautical and automobile industries. Formulations of shell finite element models are quite complex compared to other structural elements, and, not surprisingly, over the past several decades, many hundreds of papers have appeared on the subject of shell finite element analysis. We refer to older^{1,2} and recent^{3,4} reviews.

An important application for models of dynamic (transient) response of structures, including thin-walled structures conducive to representation as shells, are guided waves as used in Structural Health Monitoring^{5,6,7}. The finite element method (FEM) provides the most commonly used technique for simulation and modeling of guided waves. In the present work we illustrate the performance of our approach on applications from the guided-wave domain. Note well: This should not be construed as implication that the proposed methodology is only applicable in this area.

Clearly, traditional finite element techniques are not the only suitable technology in this application domain. The 10-20 elements per wavelength commonly recommended to achieve decent results, demand efficient, fast-running models⁸. The Spectral Element Method (SEM) is promising, as it can theoretically deliver high accuracy, aided by the nodal numerical integration rules that can produce diagonal mass matrices⁹. Finite Difference (FD) methods in the form of the Local Interaction Simulation Approach (LISA) represent another recently developed promising model^{10,11,12,13}. Parallel computational implementation of LISA for Lamb wave simulation in structures with complex geometry using graphical processing units (GPU) can lead to substantial speedups¹⁴.

The Belytschko-Lin-Tsay shell¹⁵ is in many respects still leading the pack of explicit finite element formulations¹⁶. There have been incremental improvements, of course¹⁷, and radical departures such as triangular shells with discrete Kirchhoff

constraints¹⁸, or quadrilaterals with membrane response incorporating drilling degrees freedom¹⁹. The shell finite element technology also keeps developing to incorporate modern computing devices^{20,16}. There is a creative tension between two approaches: perform a lot of numerical calculations with limited data movement²¹, or perform very simple numerical operations on a large number of simple entities²². The presented methodology belongs in the second camp.

A flat facet finite element with three nodes and six degrees of freedom per node for linear static and dynamic analysis of thick and thin shells was presented in a preceding publication²³. The membrane response was modeled with constant strain triangles and the bending response and the transverse shear were treated with an improved version of the discrete-shear-gap technique. The main novelty of that approach was the robust treatment of the drilling rotations. The drilling degrees of freedom were decoupled from the bending and twisting, and from each other. The element was shown to be robust for extremely thin shells, and passed challenging tests such as the Raasch hook problem and the hyperbolic paraboloid test. Performance was illustrated with static and free-vibration examples, including branched and folded shells.

The decoupling of the drilling degrees of freedom from the dynamical balance equations prompted an investigation into the possibility of using the flat-facet shell finite element in the simulations of linear fast transient waves in shells (guided waves) using explicit integration techniques. The plan for the current article is to very briefly review the formulation of the model of linear wave propagation in shell structures and the algorithm of explicit time stepping in Section 1. For easy reference we summarize the formulation of the elastic properties of the triangular finite elements in Section 2. Then, in Section 3, we rephrase the main points of the element basis to nodal basis to global basis transformations that will decouple the internal forces from the drilling degrees of freedom. That will prepare the ground for a discussion of the element mass matrix, selection of the parameters for the drilling degrees of freedom (stiffness and mass), and the effects of that choice on the explicit time integration algorithm. Finally, the properties of the present formulation are illustrated on a number of transient dynamics problems in Section 4. In addition to benchmark comparisons, we also demonstrate use in guided-wave simulations, including scattering from flaws. Finally, in the Conclusions we offer some remarks on potential future extensions. The reader should understand the present paper as a step on the path to a more general nonlinear capability.

1 | EXPLICIT DYNAMICS OF LINEAR WAVE PROPAGATION IN SHELL STRUCTURES

Direct time integration is widely used in finite element solutions of structural dynamics and transient wave propagation problems²⁴. There are two categories: explicit and implicit methods. A time integration method is implicit if the solution procedure requires the solution of a coupled system of equations. In an explicit method, the solution of a coupled system of equations is avoided. Implicit methods require a much larger computational effort per time step when compared with explicit methods, but implicit methods can be designed to have unconditional stability in linear analysis, and hence the time step size can be selected based on the characteristics of the problem to be integrated. Explicit methods may require only vector calculations and the computational cost per time step is consequently much lower, but an explicit method can be only conditionally stable (the condition being the length of the time step that can be taken without the solution blowing up). As a consequence, explicit methods may be effective when the time step size required by the stability limit is similar to the time step size needed to describe the physical problem. This is typically the case in wave propagation analyses.

After discretization in space with finite elements, the dynamic balance equation (Newton's equation) of linear wave propagation may be stated as

$$\mathbf{M}\mathbf{A} = \mathbf{F} - \mathbf{K}\mathbf{U} - \mathbf{C}\mathbf{V}, \quad (1)$$

where \mathbf{A} is the vector of accelerations, \mathbf{U} and \mathbf{V} are the vectors of displacements and velocities respectively, and \mathbf{M} , \mathbf{K} , and \mathbf{C} are the mass, (symmetric) stiffness, and damping matrices. The initial value problem is solved starting from the initial displacements and velocities, i.e. $\mathbf{U}(t = 0)$, $\mathbf{V}(t = 0)$ are given.

There are many suitable explicit-integration algorithms used in structural wave propagation problems^{25,26,27,24,28,29}. In this work we only apply the commonly used centered difference method. There are several possible re-formulations, cited for instance in Reference 26, and Algorithm 1 describes a variant particularly efficient with a diagonal damping matrix, which is what we assume in the examples below.

Algorithm 1 runs with a fixed time step. The time step needs to be as long as possible, for accuracy reasons, yet as short as necessary to prevent the solution from blowing up. The classical bound is provided by the estimate³⁰

$$\Delta t \leq \frac{2}{\max \omega_j}, \quad (2)$$

Algorithm 1 Algorithm “Centered Difference Explicit Integration”.

Require: Stiffness matrix \mathbf{K} , diagonal mass matrix \mathbf{M} , diagonal damping matrix \mathbf{C} , initial displacement vector \mathbf{U} , initial velocity vector \mathbf{V} , loading vector \mathbf{F} , time step Δt , number of steps to take n .

```

 $\tilde{\mathbf{M}} = \mathbf{M} + (\Delta t/2)\mathbf{C}$                                 ▷ Compute effective left hand side matrix,  $\tilde{\mathbf{M}}$ 
 $t=0$                                                         ▷ Initialize time
 $\tilde{\mathbf{M}}\mathbf{A} = \mathbf{F}(t)$                                 ▷ Compute initial acceleration,  $\mathbf{A}$ 
for  $s \in 1 : n$  do                                       ▷ For all time steps
     $t += \Delta t$                                          ▷ Update the time
     $\mathbf{U} += \mathbf{V} + ((\Delta t^2)/2)\mathbf{A}$                  ▷ Update displacements
     $\mathbf{L} = \mathbf{F}(t) - \mathbf{K}\mathbf{U} - \mathbf{C}(\mathbf{V} + (\Delta t/2)\mathbf{A})$    ▷ Update right hand side vector
     $\mathbf{V} += (\Delta t/2)\mathbf{A}$                                ▷ Update velocity with the previous acceleration
     $\mathbf{A} = \mathbf{L}/\tilde{\mathbf{M}}$                                    ▷ Update acceleration
     $\mathbf{V} += (\Delta t/2)\mathbf{A}$                                ▷ Update velocity with the current acceleration
end for

```

Here $+=$ represents an incrementation operator where the vector expression on the right is added to the destination vector on the left. The symbolically-expressed solution of the equations for the new acceleration are an elementwise division of two vectors, $A_d = L_d/\tilde{M}_{dd}$ for all degrees of freedom d .

where $\max\omega_j$ is the algebraically largest angular frequency of the undamped free vibration problem

$$-\omega_j^2 \mathbf{M} \boldsymbol{\phi} = -\mathbf{K} \boldsymbol{\phi} . \quad (3)$$

In this work, we solve for $\max\omega_j$ by applying the power method to equation (3). It is quite quick and accurate. We only consider Rayleigh mass-proportional damping, in which case the damping matrix reads

$$\mathbf{C} = 2\omega_d \xi \mathbf{M} . \quad (4)$$

Here ω_d is a fixed frequency at which an appropriate value of the critical-damping ratio ξ was determined. Note that this form of the damping matrix does not affect the stable time step.

In order to apply Algorithm 1, the discrete finite element model needs to be derived. In the next section we will describe the elastic properties of the shell finite element. Then, the handling of the drilling degrees of freedom will be discussed in detail.

2 | PROPERTIES OF THE ELEMENT IN ITS FRAME

The properties of the elastic stiffness of the flat-facet triangular shell element have been developed in detail in Reference 23. We shall only repeat a few key relations.

2.1 | Element cartesian frame basis vectors

As shown in Figure 1, the element carries a frame (basis) attached at its centroid, defined by the two nodes 1 and 2 which determine the direction of the local x_1 axis. The normal is evidently determined by the plane of the triangle. The two coordinates given by the basis vectors \mathbf{E}_1 and \mathbf{E}_2 are referred to as x_1 and x_2 . The elastic properties of the flat facet shell element are entirely expressed in this local element basis.

We write $[Q]_B$ to indicate that the quantity Q is expressed on the cartesian basis \mathbf{B} . In this work we formulate the global degrees of freedom in the *global cartesian basis* where \mathbf{G}_j is the j -th basis vector. The *element-attached basis* \mathbf{E} is expressed in the global cartesian basis \mathbf{G} as

$$[\mathbf{E}]_G = [[\mathbf{E}_1]_G, [\mathbf{E}_2]_G, [\mathbf{E}_3]_G] . \quad (5)$$

Here $[\mathbf{E}_3]_G$ is the normal to the element surface expressed on the global cartesian basis \mathbf{G} .

2.2 | Degrees of freedom

We assume three translations and three rotations per node, so that the 18 degrees of freedom of the triangle on the element basis \mathbf{E} are

$$[\mathbf{q}]_E = \begin{bmatrix} [{}^1\mathbf{q}]_E \\ [{}^2\mathbf{q}]_E \\ [{}^3\mathbf{q}]_E \end{bmatrix}, \quad (6)$$

where the nodal degrees of freedom consist of displacements \mathbf{d} and rotations \mathbf{r}

$$[{}^k\mathbf{q}]_E = \begin{bmatrix} [{}^k\mathbf{d}]_E \\ [{}^k\mathbf{r}]_E \end{bmatrix}. \quad (7)$$

The rotation components are described with the right hand side rule: positive when turning about the axis with the thumb pointing along the axis, and the fingers describing the turning direction. The rotation $[{}^k\mathbf{r}_3]_E = [{}^k\theta_3]_E$, the so called drilling degree of freedom (dof), is not associated with any stiffness at the element level. Hence, as the rotation about the normal is not associated with a physical response of the element, we may also refer to this element as a 5-dof per node element. However, for convenience we preserve the 6 dof per node form of the elementwise matrix. One of the benefits is that the transformation matrices are all square.

2.3 | Elementwise stiffness matrix

The overall stiffness 18×18 matrix of the element in the local element coordinates is

$$[\mathbf{K}]_E = [\mathbf{K}^m]_E + [\mathbf{K}^b]_E + [\mathbf{K}^s]_E, \quad (8)$$

where the constituent parts are $[\mathbf{K}^m]_E$ for the membrane response, $[\mathbf{K}^b]_E$ for the bending, and $[\mathbf{K}^s]_E$ for the transverse shear response. This stiffness matrix has a rank of 8, and hence it is rank-deficient: it has six rigid body modes, one higher order torsional zero-energy mode³¹, and three zero energy modes due to the drilling rotations not being associated with any stiffness.

The torsional mode corresponds to the rotation of the bottom surface of the shell relative to the top surface about the normal to the element surface. The torsional mode is uncoupled from the flexural modes³¹, and it is incommunicable in meshes of more than two connected triangles. The drilling rotation degrees of freedom will be treated in the next section.

3 | HANDLING OF THE DRILLING ROTATIONS

In order to remove the rank defect of the element stiffness matrix to ensure an appropriate rank of the global stiffness matrix and also to handle the transfer of the twisting moments between elements, the element formulation proposed in Reference 23 introduced a third basis, the *nodal normal basis*.

First, what is meant by a “normal”? In this context, we mean by a *nodal normal* a direction which is either the *exact normal* to the original smooth surface (as opposed to the discrete triangular approximation to it) at the location of the node, or it is an *approximation* of the exact normal, most likely derived by weighted averaging of the normals from each element connected to the node.

At each node that can be uniquely associated with a nodal normal, all the connected elements will agree on this nodal normal. At nodes at which a unique normal cannot be defined (where it does not make sense), such as at folds (creases), or along branching curves where multiple sheets of the shell meet, the connected elements will only refer to their own normal instead of the nodal normal.

At nodes with a valid (unique) nodal normal, the connected finite elements will set up an ad hoc basis. Figure 1 shows that the nodal normals at the nodes will in general be different from the normals to the elements connected at the node.

When calculating the elementwise matrices (stiffness or mass) of any given element, Cartesian coordinate basis ${}^k\mathbf{A}$ is constructed for each of the three nodes of the element such that the basis vector $[{}^k\mathbf{A}_3]_E$ at node k coincides with the normal at the node k : $[{}^k\mathbf{A}_3]_E = [{}^k\mathbf{n}]_E = [\mathbf{E}]_G^T [{}^k\mathbf{n}]_G$. Here we assume that when the nodal normal is not unique at a node j , for the purpose of the calculations on the element this normal is replaced with the element normal, $[{}^j\mathbf{A}_3]_E = [{}^j\mathbf{n}]_E = [\mathbf{E}_3]_E = [0, 0, 1]^T$.

The remaining Cartesian basis vectors of the nodal basis are obtained by rotating the element frame $[\mathbf{E}]_E = [\mathbf{1}]$ through the angle ϕ subtended by $[{}^k\mathbf{n}]_E$ and $[\mathbf{E}_3]_E$. (Refer to Figure 1.) Hence, the vectors $[{}^k\mathbf{A}_1]_E$ and $[{}^k\mathbf{A}_2]_E$ are obtained from $[\mathbf{E}_1]_E$ and

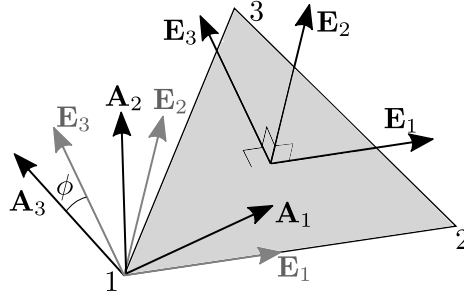


FIGURE 1 Nodal cartesian basis produced by rotation of the element basis so that the rotated element normal coincides with the nodal normal.

$[\mathbf{E}_2]_E$ by rotating through the rotation vector $\boldsymbol{\phi} = [\mathbf{E}_3]_E \times [{}^k\mathbf{A}_3]_E$, i.e.

$$[{}^k\mathbf{A}_j]_E = [\exp(\boldsymbol{\phi})]_E [\mathbf{E}_j]_E. \quad (9)$$

As a result, each element has three bases defined at its nodes, in general different for each node k

$$[{}^k\mathbf{A}]_E = [{}^k[\mathbf{A}_1]_E, {}^k[\mathbf{A}_2]_E, {}^k[\mathbf{A}_3]_E]. \quad (10)$$

Each element connected to a given node will compute for this node a different set of basis vectors (10). These different bases *will however agree* on the direction of the third vector, ${}^k\mathbf{A}_3 = {}^k\mathbf{n}$, provided the nodal normal at node k is unique.

3.1 | Stiffness matrix

The transformation of the elements stiffness matrix now proceeds in two steps²³. In the first step, we transform the element stiffness matrix into the nodal basis using the transformation

$$[\mathbf{K}]_A = [\mathbf{T}^A]_E^T [\mathbf{K}]_E [\mathbf{T}^A]_E. \quad (11)$$

The transformation matrix $[\mathbf{T}^A]_E$ takes as input a vector in the nodal basis (\mathbf{A}) and outputs a vector in the element basis (\mathbf{E}). We construct the 3×3 matrices

$$[{}^k\tilde{\mathbf{A}}]_E = \begin{bmatrix} [{}^k\mathbf{A}_{1:2,1:2}]_E - [{}^k\mathbf{A}_{3,3}]_E^{-1} [{}^k\mathbf{A}_{1:2,3}]_E [{}^k\mathbf{A}_{3,1:2}]_E & \mathbf{0} \\ \mathbf{0} & \mathbf{0} \end{bmatrix} \quad (12)$$

and

$$[{}^{kj}\tilde{\mathbf{X}}]_E = \begin{bmatrix} [{}^k\mathbf{A}_{3,3}]_E^{-1} [{}^k\mathbf{A}_{1:2,3}]_E \frac{1}{2} \sum_j \left(\frac{\partial^j N}{\partial x_1} [\mathbf{E}_2]_E^T - \sum_j \frac{\partial^j N}{\partial x_2} [\mathbf{E}_1]_E^T \right) [{}^k\mathbf{A}]_E \\ \mathbf{0} \end{bmatrix} \quad (13)$$

where we use the notation $[\mathbf{A}_{3,1:2}]_E$ to designate a sub-matrix consisting of the row 3 and the columns 1 and 2 of the matrix $[\mathbf{A}]_E$ and so on. With these definitions, we can write a transformation matrix from the nodal basis into the element basis as

$$[\mathbf{T}^A]_E = \begin{bmatrix} [{}^1\mathbf{A}]_E & \mathbf{0} & \mathbf{0} & \mathbf{0} & \mathbf{0} & \mathbf{0} \\ [{}^{11}\tilde{\mathbf{X}}]_E & [{}^1\tilde{\mathbf{A}}]_E & [{}^{12}\tilde{\mathbf{X}}]_E & \mathbf{0} & [{}^{13}\tilde{\mathbf{X}}]_E & \mathbf{0} \\ \mathbf{0} & \mathbf{0} & [{}^2\mathbf{A}]_E & \mathbf{0} & \mathbf{0} & \mathbf{0} \\ [{}^{21}\tilde{\mathbf{X}}]_E & \mathbf{0} & [{}^{22}\tilde{\mathbf{X}}]_E & [{}^2\tilde{\mathbf{A}}]_E & [{}^{23}\tilde{\mathbf{X}}]_E & \mathbf{0} \\ \mathbf{0} & \mathbf{0} & \mathbf{0} & \mathbf{0} & [{}^3\mathbf{A}]_E & \mathbf{0} \\ [{}^{31}\tilde{\mathbf{X}}]_E & \mathbf{0} & [{}^{32}\tilde{\mathbf{X}}]_E & \mathbf{0} & [{}^{33}\tilde{\mathbf{X}}]_E & [{}^3\tilde{\mathbf{A}}]_E \end{bmatrix}_E. \quad (14)$$

The transformation (11) accomplishes the following: the drilling rotations about the nodal normals are now totally decoupled from the elastic response of the element (note that the third column of (12) consists only of zeros!). This is true for *all* elements connected at a node. This is an important point, as the drilling rotations expressed about the normal to any particular element

are *only* decoupled from the elastic response of *that element*, but in general would be coupled to any other non-coplanar adjacent element.

So, to stress this point, rotations about the nodal normals are now totally independent individual degrees of freedom, not only for the single finite element at hand, but globally. At the moment, these degrees of freedom are not associated with any stiffness at all. However, we can remedy this situation by adding an arbitrary stiffness on the diagonal of $[\mathbf{K}]_A$: we add a torsional stiffness $k_d > 0$ to the drilling degrees of freedom on the nodal basis

$$[\mathbf{K}_{6,6}]_A = k_d, \quad [\mathbf{K}_{12,12}]_A = k_d, \quad [\mathbf{K}_{18,18}]_A = k_d. \quad (15)$$

The rank of the element stiffness matrix at this point increases to 11, which may be considered a full rank (the twisting mode is not communicable). Next, the matrix (11) is transformed into the global cartesian coordinate system

$$[\mathbf{K}]_G = [\mathbf{T}^G]_A^T [\mathbf{K}]_A [\mathbf{T}^G]_A \quad (16)$$

where the transformation matrix $[\mathbf{T}^G]_A$ takes as input a vector in the global cartesian coordinate system (\mathbf{G}), and outputs a vector in the nodal coordinate basis (\mathbf{A}):

$$[\mathbf{T}^G]_A = \begin{bmatrix} [{}^1\mathbf{A}]_E^T [\mathbf{E}]_G^T & \mathbf{0} & \mathbf{0} & \mathbf{0} & \mathbf{0} & \mathbf{0} \\ \mathbf{0} & [{}^1\mathbf{A}]_E^T [\mathbf{E}]_G^T & \mathbf{0} & \mathbf{0} & \mathbf{0} & \mathbf{0} \\ \mathbf{0} & \mathbf{0} & [{}^2\mathbf{A}]_E^T [\mathbf{E}]_G^T & \mathbf{0} & \mathbf{0} & \mathbf{0} \\ \mathbf{0} & \mathbf{0} & \mathbf{0} & [{}^2\mathbf{A}]_E^T [\mathbf{E}]_G^T & \mathbf{0} & \mathbf{0} \\ \mathbf{0} & \mathbf{0} & \mathbf{0} & \mathbf{0} & [{}^3\mathbf{A}]_E^T [\mathbf{E}]_G^T & \mathbf{0} \\ \mathbf{0} & \mathbf{0} & \mathbf{0} & \mathbf{0} & \mathbf{0} & [{}^3\mathbf{A}]_E^T [\mathbf{E}]_G^T \end{bmatrix}. \quad (17)$$

After we assemble the matrices (16), the global stiffness matrix no longer has zero-eigenvalue eigenvectors corresponding to rotations about the nodal normals.

3.2 | Mass matrix

The explicit time integration algorithm requires a diagonal global mass matrix for efficiency. The element mass matrix can be easily constructed on the element basis \mathbf{E} as diagonal using a nodal integration rule (three integration points per triangle located at the nodes). The diagonal elements corresponding to *translations* are

$$[\mathbf{M}_{ii}]_E = \int_A {}^k N^2 t \rho dA, \quad (18)$$

where the translation degree of freedom i is located at node k , t is the uniform thickness of the element, A is the area of the triangle, and ρ is the mass density. The integral is evaluated as

$$[\mathbf{M}_{ii}]_E \approx \frac{At\rho}{3}, \quad (19)$$

i.e. as one third of the total mass of the element.

The diagonal elements corresponding to *flexural rotations* of the nodes can be evaluated using the moment of inertia density³², again using nodal quadrature, as

$$[\mathbf{M}_{ii}]_E = \int_A {}^k N^2 \frac{t^3}{12} \rho dA \approx \frac{At^3\rho}{36}. \quad (20)$$

where the flexural-rotation degree of freedom i (i.e. $i = 4, 5, 10, 11, 16, 17$ on the element level) is located at node k .

Finally, we need to assign some inertial properties to the *drilling-rotation* degrees of freedom. Leaving these generalized masses as zero is not an option, as that would lead to infinite frequencies in the vibration spectrum, which would destroy the explicit time integration.

There is also the consideration of the need to transform the element matrix into the global cartesian coordinate system \mathbf{G} . For each node k , the submatrix of the mass matrix corresponding to translations is a multiple of the identity, where $At\rho/3$ is the multiplier. This submatrix is expressed on the element basis \mathbf{E} , but the transformation leaves it alone, i.e. the submatrix transformed into the global basis \mathbf{G} is the same scaled identity. Therefore, if we wish to preserve the same property for the

rotations, we simply make the drilling-rotation mass coefficient the same as the flexural-rotation mass coefficients, that is we use (20) for $i = 6, 12, 18$. Thus, the mass matrix of a single element adopted here is

$$[\mathbf{M}]_{E,G} = \begin{bmatrix} \frac{At\rho}{3} [\mathbf{1}] & \mathbf{0} & \mathbf{0} & \mathbf{0} & \mathbf{0} & \mathbf{0} \\ \mathbf{0} & \frac{At^3\rho}{36} [\mathbf{1}] & \mathbf{0} & \mathbf{0} & \mathbf{0} & \mathbf{0} \\ \mathbf{0} & \mathbf{0} & \frac{At\rho}{3} [\mathbf{1}] & \mathbf{0} & \mathbf{0} & \mathbf{0} \\ \mathbf{0} & \mathbf{0} & \mathbf{0} & \frac{At^3\rho}{36} [\mathbf{1}] & \mathbf{0} & \mathbf{0} \\ \mathbf{0} & \mathbf{0} & \mathbf{0} & \mathbf{0} & \frac{At\rho}{3} [\mathbf{1}] & \mathbf{0} \\ \mathbf{0} & \mathbf{0} & \mathbf{0} & \mathbf{0} & \mathbf{0} & \frac{At^3\rho}{36} [\mathbf{1}] \end{bmatrix}_{E,G}. \quad (21)$$

Herein we use the subscript E, G to indicate that the lumped mass matrix has exactly the same form in the element coordinates as in the global cartesian coordinates.

Adopting the same mass coefficient for the drilling rotations as for the flexural rotations may seem strange, or at least physically unmotivated. However, the drilling degrees of freedom are *uncoupled* from each other and from all the other degrees of freedom in the system. Therefore, they will *not contribute to the dynamics* of the system. The mass coefficient for the drilling degree of freedom can therefore be set to an arbitrary value, and we use that device here to make the construction of a diagonal mass matrix easy.

3.3 | Control of the stable time step

Recall that the transformation of the element stiffness matrices elastically decoupled all drilling degrees of freedom from the other degrees of freedom in the dynamical system of the balance equations. Therefore, all drilling degrees of freedom represent single-degree-of-freedom torsional oscillators, were the mass is assembled from the element mass matrices (21), and the torsional stiffness are the coefficients k_d assembled from the elements. Reference 23 suggested for the torsional stiffness coefficient the quantity

$$k_d = \zeta \times \text{mean}_{i=4,5,10,11,16,17} ([\mathbf{K}_{ii}]_E), \quad (22)$$

i.e. a multiple of the average flexural stiffness coefficient of the element. The multiplier $\zeta = 1$ was suggested based on the following considerations:

1. The multiplier should not be a very small number or a very large number in order to protect the condition number of the stiffness matrix.
2. The static response was shown to be entirely independent of the magnitude of the multiplier ζ when the exact normals could be constructed, and the value $\zeta = 1$ produced acceptable results for approximate nodal normals.
3. For free vibration analysis, the multiplier should not be so small as to make the torsional springs for the drilling degrees of freedom so soft that the natural frequencies of the system will be interspersed with (polluted by) the meaningless torsional drilling oscillations. Again, $\zeta = 1$ proved satisfactory.

For the explicit integration of transient dynamic response (wave propagation) we would add a fourth consideration:

4. For fast transient analysis with an explicit integration method, the multiplier should not be so large as to make the torsional springs for the drilling degrees of freedom so stiff that the natural frequencies of the system will be dominated by the frequencies of the torsional drilling oscillations. These unphysical frequencies would then dictate (control) the stable time step, driving it unnecessarily down.

It turns out that $\zeta = 1$ is again a good choice. To see why that is so, consider that the elastic constant for the drilling rotations is the average of the flexural stiffness coefficients. The mass coefficients for the drilling rotations are also averages of all the rotation (moment of inertia) mass-matrix coefficients. Therefore, it makes sense to expect that the natural frequencies corresponding to pure flexure will be similar to those for the drilling rotations.

Consider a sample wave propagation simulation, in a cylindrical shell of radius R and thickness t . Figure 2 provides some data to illustrate the consequences of choosing ζ differently: The vertical axis is the normalized time step, where the time step used for

the normalization is the longest possible one. The horizontal axis are the values of the multiplier ζ . Making ζ smaller decreases the global natural frequencies corresponding to drilling rotations, and the time step is controlled by the highest meaningful physical frequency. If we select $\zeta > 1.5$, the natural frequencies corresponding to drilling rotations will start to dominate the spectrum of the generalized eigenvalue pencil, and the critical time step will be controlled by them. For $\zeta = 10$, the stable time step will have dropped to 40% of the longest possible time step. The graph shows multiple curves to illustrate the dependence of the stable time step on the thickness of the shell expressed with the aspect ratio t/R .

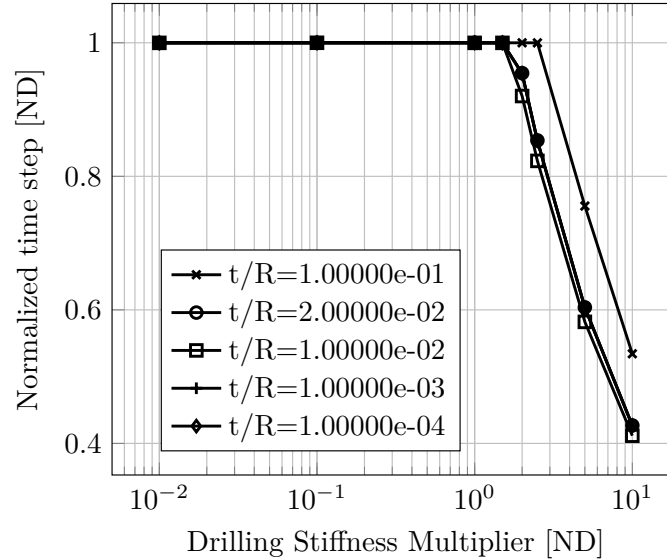


FIGURE 2 The stable time step for the cylindrical shell as a function of the drilling stiffness multiplier ζ , for various thickness to radius ratios.

For the explicit dynamics of shells, the item 3. considered above actually is not critical. Because the drilling rotations are mutually uncoupled, and also decoupled from all physical degrees of freedom, they will not get excited (if no loading is applied directly to the drilling degrees of freedom, which should not be allowed in our opinion). Figure 3 demonstrates that the kinetic energy is unaffected by choosing three different values of the drilling stiffness multiplier ζ – the three curves overlap. The only effect is a stable time step reduction for $\zeta = 10$.

4 | NUMERICAL EXAMPLES

The computations with the present model were implemented in the Julia programming language^{33,34}, in the framework of the `FinEtoolsFlexStructures.jl` Julia package³⁵. The results reported below can be reproduced with the `TestT3FFExplicit.jl` Julia package (refer to the data section).

4.1 | Spherical cap shell with suddenly applied pressure loading

This example is as close as we can come to an established benchmark for transient-vibration simulation. The first solution was apparently published by Bathe et al.³⁶, and the solution was obtained with quadratic axisymmetric shell elements. The benchmark configuration is described in Figure 4. The material of the shell had Young's modulus $E = 10.5 \times 10^6$ psi, Poisson's ratio $\nu = 0.3$, and mass density $\rho = 2.45 \times 10^{-4}$ lb s²/in⁴. The shell was 0.41 in thick. The loading was 600 psi uniform pressure applied from the top in the form of a step function.

In addition to the results of Bathe et al.³⁶, we also consider our own simulation with Abaqus³⁷ quadrilateral small-strain elements (S4R5), with an implicit time stepping (labeled A/impl), and the small-strain quadrilateral with warping improvements (S4RSW), with explicit time stepping (label A/expl).

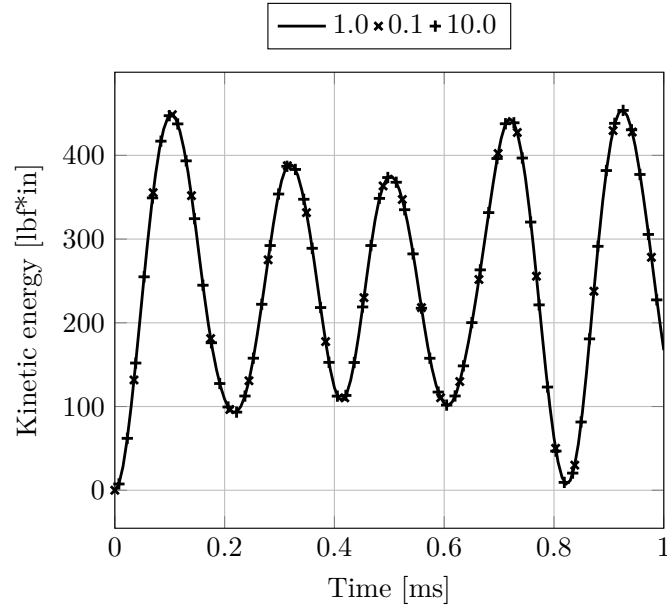


FIGURE 3 Spherical cap. Kinetic energy obtained for three different values of the drilling stiffness multiplier ζ . The three curves coincide: the drilling degrees of freedom do not contribute to the kinetic energy.

The present mesh consisted of 397 nodes, and 726 triangular elements, which is approximately the same mesh as in the Abaqus simulations, and the vibration event of 1 ms duration was advanced in 945 steps. The agreement with the three reference solutions listed above is quite satisfactory.

We have omitted in this comparison for instance References 15 and 38, because their results are quite different from the four curves presented in Figure 5 (*none* of the four curves are matched). The References 39,40 were also disregarded because the data in these articles were found to be in error (the angle was listed as 22.67° , probably by mistake).

4.2 | Elastic Waves in a Thin Aluminum Plate

The monograph by Ostachowicz et al.⁹ presents a useful collection of examples of wave propagation in plates and shells. In this section we shall consider wave propagation in a plate. For this example the book provides both a computational result and experimental data allowing for both verification and validation.

The structure was a square aluminum plate, one quarter of which was modeled using two symmetry planes (refer to Figure 6). The side length of the plate was $L = 1000\text{mm}$, while its thickness h was 1mm. The excitation was a concentrated force at the center in the form of a Hann-windowed sinusoidal signal, where the carrier frequency was 35kHz and its modulation frequency was 7kHz. The material of the plate was aluminum alloy with Young's modulus $E = 68.0\text{ GPa}$, Poisson's ratio $\nu = 0.33$, and mass density $\rho = 2660\text{ kg/m}^3$.

Experimental measurements obtained with laser scanning vibrometry were reported. The laser scanning measurements were based on a grid of 225×227 points covering one-quarter of the plate, taken at 1024 time snapshots within the first 1 ms of response. The wave propagation patterns represented the A_0 mode (transverse flexural vibration). The time interval was sufficiently long to introduce reflections of the propagating waves from the plate boundaries.

The computational model consisted of a regular arrangement of triangular shell elements, with equal number of nodes along both directions. The meshes used in this investigation are listed in Table 1. Mass-proportional damping was applied with the fraction of critical damping set to $\xi = 7.95775 \times 10^{-3}$, and with $\omega_d = 2000\pi$. Even though the problem represents a plate, all six degrees of freedom per node have been employed in order to test thoroughly the present formulation for flat geometries.

Figure 7 shows three snapshots of the computed displacements. These can be compared directly with the numerical simulations and the experimentally acquired laser scanning vibrometry images in Figure 5.20 of the Reference 9. The agreement is very good.

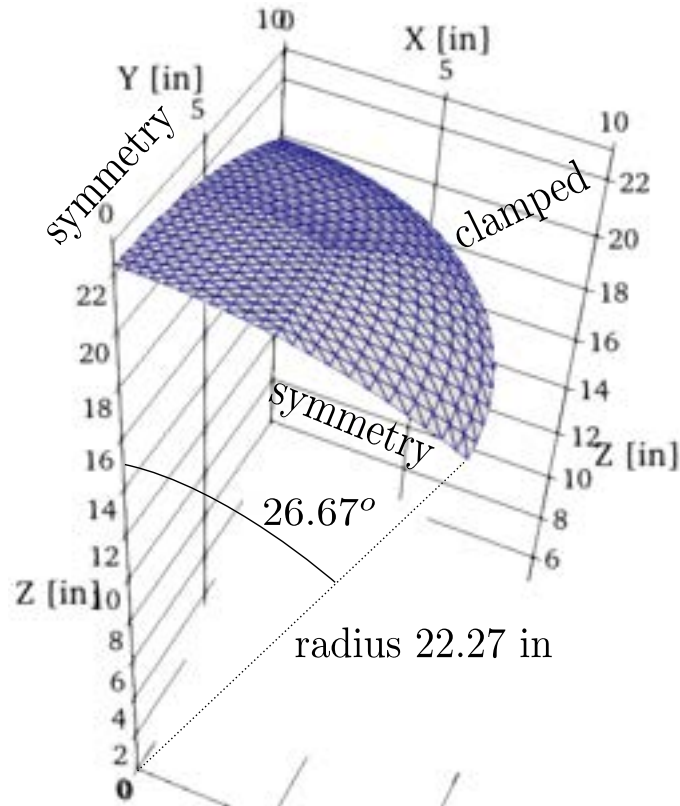


FIGURE 4 Spherical cap, mesh with 22 element edges along the radius.

TABLE 1 Free-floating plate with center loading. Meshes employed in Figure 9.

Mesh	(a)	(b)	(c)
Number of nodes [ND]	25921	103041	410881
Number of elements [ND]	51200	204800	819200
Element size [mm]	3.12500	1.56250	0.78125
Number of time steps [ND]	3345	5902	10846
Run time [s]	12.6	93	752

Figure 8 shows the computed velocity perpendicular to the plane of the plate (transverse) at point *C*. The first wave packet from the left is the arrival of the loading pulse, the second wave packet is the arrival of the reflection from the right hand side boundary. The timings of arrival and the relative magnitudes of the wave packets are in good agreement with the experimental data⁹. Their results have been obtained with the mesh (b) of Table 1. The simulation was run on a Surface Pro tablet, and executed in less than two minutes using 4 concurrent threads.

Figure 9 addresses convergence of the computed response at point *C* with refinement. The velocity was computed for three meshes (refer to Table 1). There is an appreciable difference between the coarsest mesh (a) and the two finer meshes, but very little difference between meshes (b) and (c).

The numerical results reported in Reference 9 have been obtained with spectral plate finite elements of fifth order. The number of elements was 10240, so almost 20 times smaller than in our mesh (b), but the number of time steps required in Reference 9 was 50,000, so roughly 8 times more than for our mesh (b). Also, the number of nodes in the fifth-order spectral method is on the order of 25× the number of elements, whereas the number of nodes in the present method is only around one half of the number of elements. The relative accuracy of the computed response cannot be ascertained, but qualitatively the results obtained in the present work compare favorably with Figure 5.21 of Reference 9.

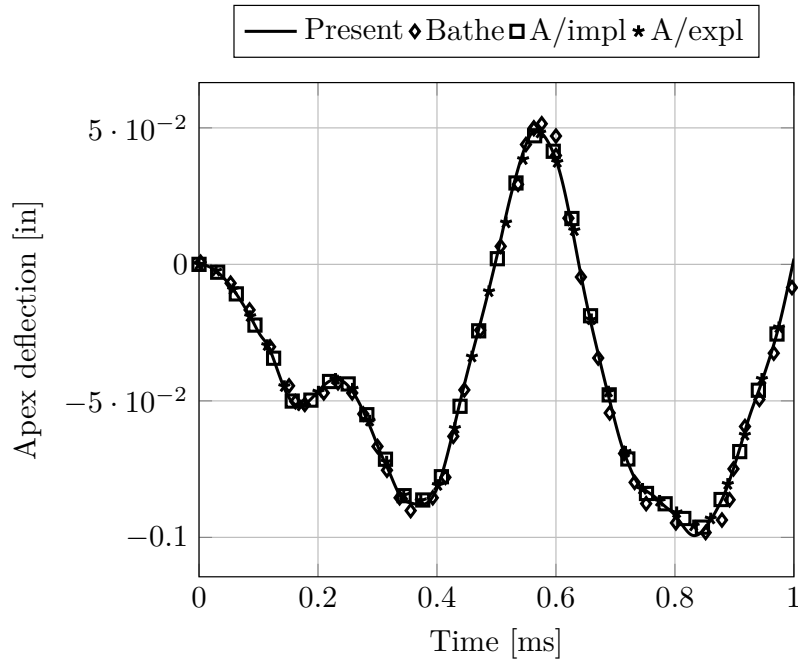


FIGURE 5 Spherical cap, mesh with eight element edges along the radius.

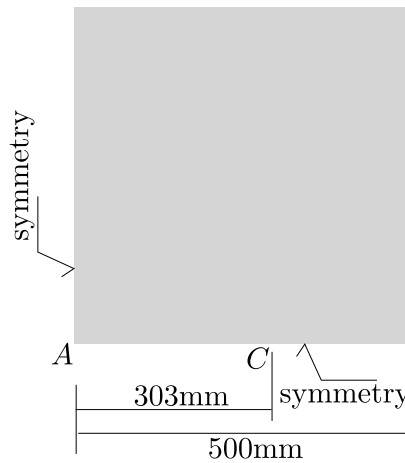


FIGURE 6 Free-floating plate with center loading (point A). Symmetry conditions applied along two sides of the quarter plate, the other two sides are free. Transverse velocity at point C is measured.

4.3 | Elastic Waves in a Folded Shell

The monograph by Ostachowicz et al.⁹ describes wave propagation in an aluminum bar of an L-shape cross section, refer to Figure 10. The length of the bar was $L = 1000\text{mm}$, the flanges were $W = 250\text{mm}$ wide, and the thickness of the material h was 10mm . The excitation was a concentrated force of 1.0 N at the midpoint of one of the flanges ($x = L/2$, $y = W$, $z = 0$) in the form of a Hann-windowed sinusoidal signal, where the carrier frequency was 75kHz and its modulation frequency was one quarter of the carrier frequency. The material of the plate was aluminum with Young's modulus $E = 72.7\text{ GPa}$, Poisson's ratio $\nu = 0.33$, and mass density $\rho = 2700\text{ kg/m}^3$.

Figure 11 shows the snapshots of the propagating waves. The displacements have been highly magnified, and the snapshots have been taken at $62.5\text{ }\mu\text{s}$ intervals. The conversion of the initially generated flexural wave at the crease where the flanges meet

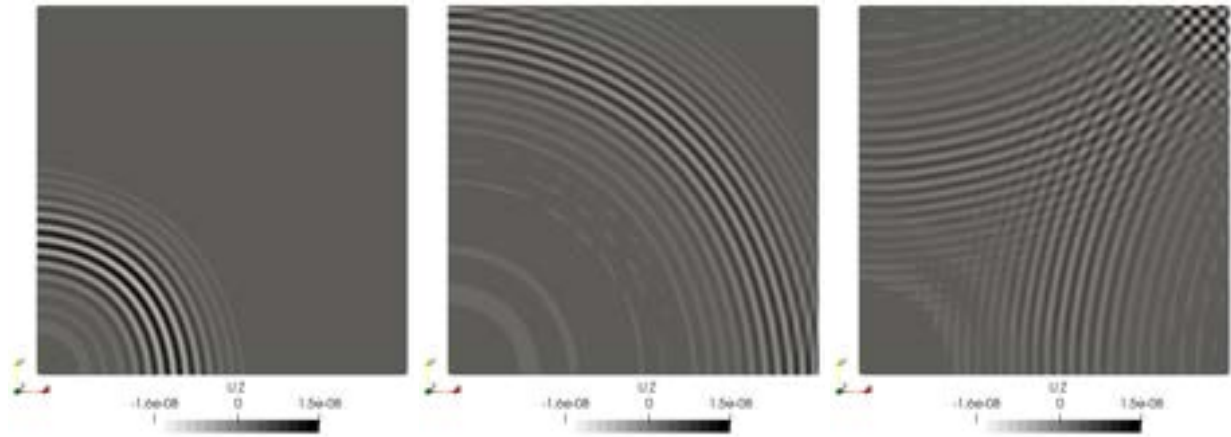


FIGURE 7 Free-floating plate with center loading. Snapshots of the transverse displacement: left to right 0.25ms, 0.5ms, 0.75ms.

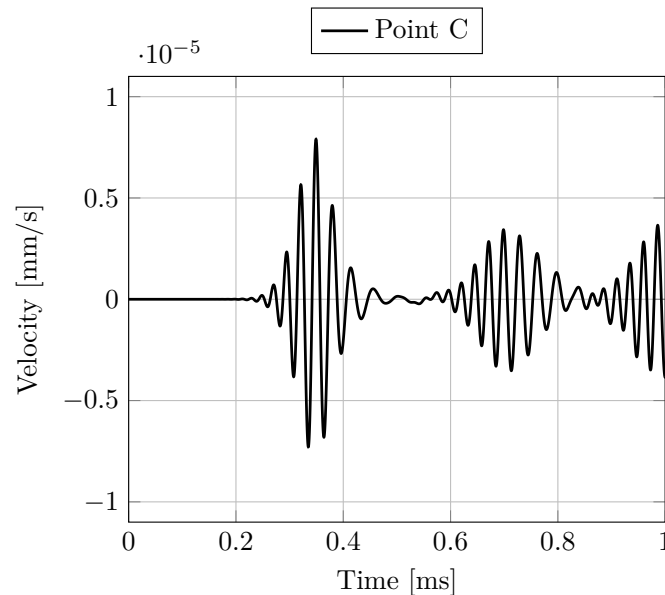


FIGURE 8 Free-floating plate with center loading. Transverse velocity at point C.

into in-plane and shear waves is notable. The displacement magnitude was color coded using the “X-ray” color map, and the snapshots agree well with Figure 5.16 of the Reference 9.

4.4 | Half-pipe Shell with an Open Crack

The monograph by Ostachowicz et al.⁹ describes wave propagation in a half-pipe aluminum shell, with details provided in Figure 12. The length of the shell was $L = 1000\text{mm}$, the circumferential dimension was $W = 500\text{mm}$, corresponding to a radius of $R = 159.155\text{mm}$, and the thickness of the material h was 10mm . The excitation was a concentrated force of 1.0N at the corner of the shell ($x = L/2$, $y = W$, $z = 0$) in the form of a Hann-windowed sinusoidal signal, where the carrier frequency was 75kHz and its modulation frequency was one quarter of the carrier frequency. The material of the plate was aluminum with Young’s modulus $E = 72.7\text{GPa}$, Poisson’s ratio $\nu = 0.33$, and mass density $\rho = 2700\text{kg/m}^3$. An open crack was located at mid-length, of angular dimension 6° and positioned 40° from the horizontal (XY) plane. A regular mesh which incorporated the crack was generated, consisting of 246864 nodes, 491520 elements. The time interval of $0.5\text{ms} = 500\mu\text{s}$ was traversed with 3713 steps.

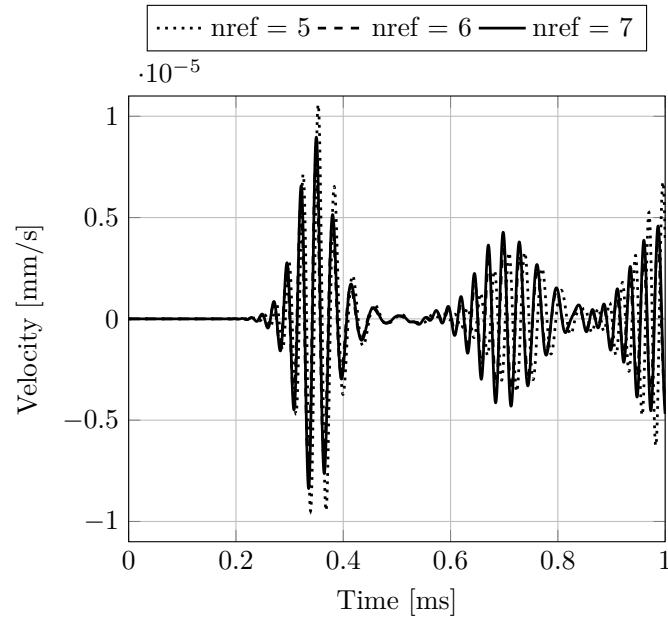


FIGURE 9 Free-floating plate with center loading. Comparison of the velocity at point *C* for three progressively finer meshes. Refer to Table 1.

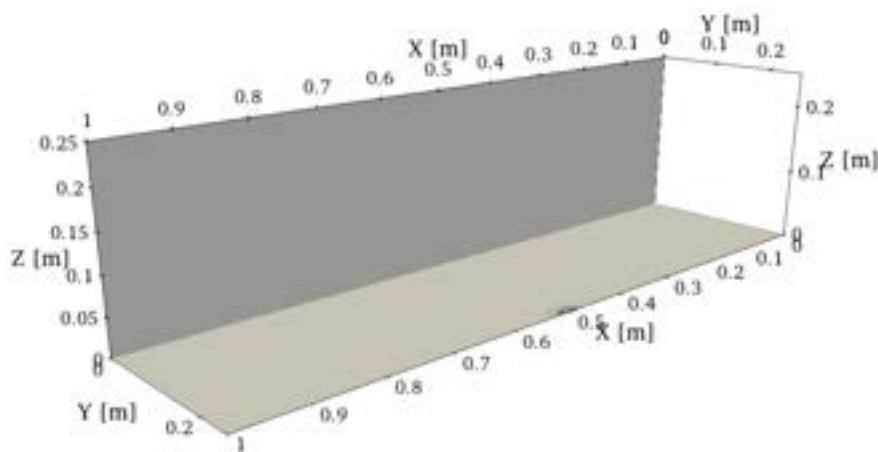


FIGURE 10 Angle bar geometry.

The propagating Lamb guided waves are illustrated in Figure 13. The displacements are highly magnified, and the peak magnitude of the displacement is color coded as dark gray color. Of particular interest are frames at $187.5 \mu\text{s}$, which shows the arriving wavefront beginning to interact with the crack, at $250.0 \mu\text{s}$, which shows the wave reflected back from the crack (towards the left and downwards in the figure), and the frame at $312.5 \mu\text{s}$, which shows the interaction of the wave scattered from the crack with the flexural wave reflected from the far straight edge of the shell.

CONCLUSIONS

We studied explicit integration of the equations of motion of thin-walled (shell-like) structures discretized with the finite element method. A flat-facet triangular finite element for shear-deformable shell structures developed in Reference 23 was applied to fast transient wave-propagation events. The element internally uses five physical degrees of freedom per node (three translations and

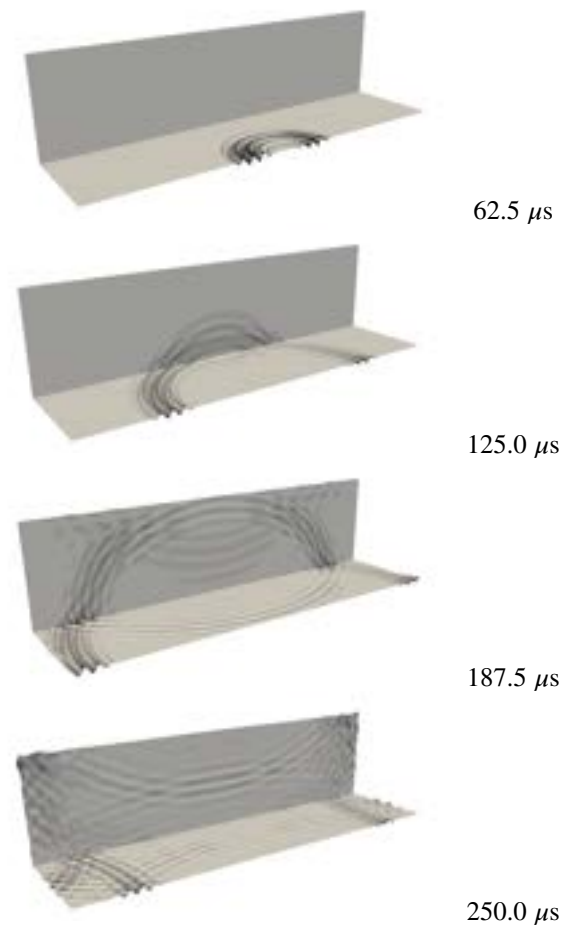


FIGURE 11 Angle bar. Snapshots of the propagating waves at 62.5 μs intervals, starting at the top from 62.5 μs , and finishing at the bottom at 250.0 μs .

two flexural rotations), but six cartesian degrees of freedom per node globally. A transformation between the element cartesian frame and the global cartesian coordinate system via an intermediate basis at the nodes wholly decouples the global drilling rotations from the elementwise flexural deformations. The global drilling rotations are independent of each other, and decoupled from the other degrees of freedom in the system. Hence, an arbitrary stiffness and mass coefficients could be applied to the drilling rotations. The goal is to prevent the singularity of the global stiffness matrix and to avoid infinite natural frequencies.

These considerations potentially affect the accuracy and stability of the time integration method. The contribution of the present work was to unravel the interdependency of the mass and stiffness parameters associated with the drilling degrees of freedom. The developed approach fixed the mass moment of inertia assembled to the global drilling degrees of freedom using the corresponding coefficients applied to the flexural degrees of freedom. The stiffness coefficient assembled from the elements in the form of a multiple of the mean stiffness coefficient from the diagonal of the elementwise stiffness matrix was then shown to contribute to the good conditioning of the stiffness matrix, as well as to keeping the artificial frequencies associated with the drilling degrees of freedom from reducing the stable time step of the explicit integration algorithm.

Numerical examples were used to illustrate the performance. Benchmark solutions were explored, as well as examples of tracking of guided Lamb waves, including reflections from flaws in shells.

Although only linear wave propagation problems were addressed, and the material of the shell was assumed homogeneous and isotropic, extensions in multiple directions are possible: The material need not be isotropic, and layered shells may be incorporated with classical theory of lamination. Inelastic response and geometrical nonlinearity are possible areas of future research.

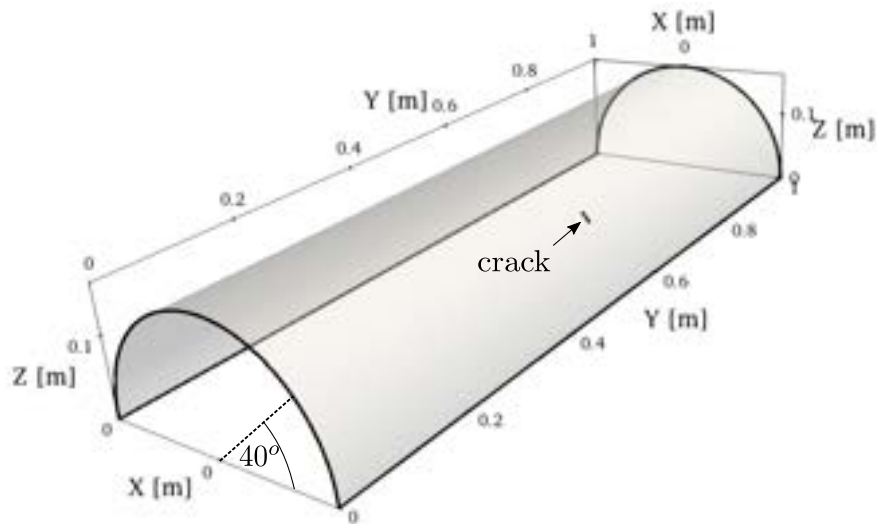


FIGURE 12 Half-pipe shell with an open crack.

ACKNOWLEDGEMENTS

Wieslaw Ostachowicz kindly provided some data to assist with the analysis of the structures referenced in the examples.

FINANCIAL DISCLOSURE

None reported.

CONFLICT OF INTEREST

The authors declare no potential conflict of interests.

DATA AVAILABILITY

The source code and data used to produce the results in this paper are freely available in the repository <https://github.com/PetrKryslUCSD/TestT3FFexplicit.jl>. The source code of the finite element formulation is available in the repository <https://github.com/PetrKryslUCSD/FinEtoolsFlexStructures.jl>.

References

1. Yang HTY, Saigal S, Masud A, Kapania RK. A survey of recent shell finite elements. *International Journal for Numerical Methods in Engineering* 2000; 47(1-3): 101-127.
2. Reddy JN, Arciniega RA. Shear deformation plate and shell theories: From Stavsky to present. *Mechanics of Advanced Materials and Structures* 2004; 11(6): 535-582. doi: 10.1080/15376490490452777
3. Irfan S, Siddiqui F. A review of recent advancements in finite element formulation for sandwich plates. *Chinese Journal of Aeronautics* 2019; 32(4): 785-798. doi: 10.1016/j.cja.2018.11.011



FIGURE 13 Half-pipe shell with an open crack. Snapshots of the propagating waves at 62.5 μs intervals, from 62.5 μs to 500.0 μs .

4. Lavrencic M, Brank B. Hybrid-Mixed Low-Order Finite Elements for Geometrically Exact Shell Models: Overview and Comparison. *Archives of Computational Methods in Engineering* 2021; 28(5): 3917-3951. doi: 10.1007/s11831-021-09537-2
5. Willberg C, Duczek S, Vivar-Perez JM, Ahmad ZAB. Simulation Methods for Guided Wave-Based Structural Health Monitoring: A Review. *Applied Mechanics Reviews* 2015; 67(1). 010803doi: 10.1115/1.4029539
6. Mitra M, Gopalakrishnan S. Guided wave based structural health monitoring: A review. *Smart Materials and Structures* 2016; 25(5): 053001. doi: 10.1088/0964-1726/25/5/053001
7. Raghavan A, Cesnik CES. Review of Guided-wave Structural Health Monitoring. *The Shock and Vibration Digest* 2007; 39: 91-114.
8. Maio L, Memmolo V, Ricci F, Boffa N, Monaco E, Pecora R. Ultrasonic wave propagation in composite laminates by numerical simulation. *Composite Structures* 2015; 121: 64-74. doi: <https://doi.org/10.1016/j.compstruct.2014.10.014>
9. Ostachowicz W, Kudela P, Krawczuk M, Zak A. *Guided Waves in Structures for SHM: The Time - domain Spectral Element Method*. A John Wiley & Sons, Ltd., publicationWiley . 2011.
10. Delsanto P, Whitcombe T, Chaskelis H, Mignogna R. Connection machine simulation of ultrasonic wave propagation in materials. I: the one-dimensional case. *Wave Motion* 1992; 16(1): 65-80. doi: [https://doi.org/10.1016/0165-2125\(92\)90047-6](https://doi.org/10.1016/0165-2125(92)90047-6)

11. Delsanto P, Schechter R, Mignogna R, Chaskelis H, Kline R. Connection machine simulation of ultrasonic wave propagation in materials. II: The two-dimensional case. *Wave Motion* 1994; 20(4): 295-314. doi: [https://doi.org/10.1016/0165-2125\(94\)90016-7](https://doi.org/10.1016/0165-2125(94)90016-7)
12. Delsanto P, Schechter R, Mignogna R. Connection machine simulation of ultrasonic wave propagation in materials III: The three-dimensional case. *Wave Motion* 1997; 26(4): 329-339. doi: [https://doi.org/10.1016/S0165-2125\(97\)00013-9](https://doi.org/10.1016/S0165-2125(97)00013-9)
13. Lee BC, Staszewski WJ. Lamb wave propagation modelling for damage detection: I. Two-dimensional analysis. *Smart Materials and Structures* 2007; 16(2): 249-259. doi: [10.1088/0964-1726/16/2/003](https://doi.org/10.1088/0964-1726/16/2/003)
14. Packo P, Kijanka P, Leamy MJ. Spectral analysis of guided wave propagation in discretized domains under local interactions. *Proceedings of the Institution of Mechanical Engineers, Part C: Journal of Mechanical Engineering Science* 2020; 234(3): 746-769. doi: [10.1177/0954406219884977](https://doi.org/10.1177/0954406219884977)
15. Belytschko T, Lin JJ, Tsay CS. Explicit algorithms for the nonlinear dynamics of shells. *Computer Methods in Applied Mechanics and Engineering* 1984; 42(2): 225-251. doi: [https://doi.org/10.1016/0045-7825\(84\)90026-4](https://doi.org/10.1016/0045-7825(84)90026-4)
16. Cai Y, Li G, Liu W. Parallelized implementation of an explicit finite element method in many integrated core (MIC) architecture. *Advances in Engineering Software* 2018; 116: 50-59. doi: <https://doi.org/10.1016/j.advengsoft.2017.12.001>
17. Key SW, Hoff CC. An improved constant membrane and bending stress shell element for explicit transient dynamics. *Computer Methods in Applied Mechanics and Engineering* 1995; 124(1): 33-47. doi: [https://doi.org/10.1016/0045-7825\(95\)00785-Y](https://doi.org/10.1016/0045-7825(95)00785-Y)
18. Wu S, Li G, Belytschko T. A DKT shell element for dynamic large deformation analysis. *Communications in Numerical Methods in Engineering* 2005; 21(11): 651-674. doi: <https://doi.org/10.1002/cnm.783>
19. Kugler S, Fotiu PA, Murin J. A highly efficient membrane finite element with drilling degrees of freedom. *Acta Mechanica* 2010; 213(3): 323-348. doi: [10.1007/s00707-009-0279-8](https://doi.org/10.1007/s00707-009-0279-8)
20. Bartezzaghi A, Cremonesi M, Parolini N, Perego U. An explicit dynamics GPU structural solver for thin shell finite elements. *Computers & Structures* 2015; 154: 29-40. doi: <https://doi.org/10.1016/j.compstruc.2015.03.005>
21. Willberg C, Eisenträger S, Perez J, Schmicker D, Gabbert U. Comparison of different higher order finite element schemes for the simulation of Lamb waves. *Computer Methods in Applied Mechanics and Engineering* 2012; 241-244: 246-261. doi: [10.1016/j.cma.2012.06.011](https://doi.org/10.1016/j.cma.2012.06.011)
22. Strbac V, Pierce D, Vander Sloten J, Famaey N. GPGPU-based explicit finite element computations for applications in biomechanics: the performance of material models, element technologies, and hardware generations. *Computer Methods in Biomechanics and Biomedical Engineering* 2017; 20: 1643-1657. doi: [10.1080/10255842.2017.1404586](https://doi.org/10.1080/10255842.2017.1404586)
23. Krysl P. Robust Flat-Facet Triangular Shell Finite Element. *International Journal for Numerical Methods in Engineering*; n/a(n/a). doi: <https://doi.org/10.1002/nme.6944>
24. Noh G, Bathe KJ. An explicit time integration scheme for the analysis of wave propagations. *Computers & Structures* 2013; 129: 178-193. doi: <https://doi.org/10.1016/j.compstruc.2013.06.007>
25. Chung J, Lee JM. A new family of explicit time integration methods for linear and non-linear structural dynamics. *International Journal for Numerical Methods in Engineering* 1994; 37: 3961-3976.
26. Krysl P, Belytschko T. Object-oriented parallelization of explicit structural dynamics with PVM. *Computers & Structures* 1998; 66(2): 259-273. doi: [https://doi.org/10.1016/S0045-7949\(97\)00065-5](https://doi.org/10.1016/S0045-7949(97)00065-5)
27. Ekevid T, Wiberg NE. A comparison of parallel implementation of explicit DG and central difference method. *Communication in Numerical Methods in Engineering* 2002; 18: 585-597.
28. Soares D. A novel family of explicit time marching techniques for structural dynamics and wave propagation models. *Computer Methods in Applied Mechanics and Engineering* 2016; 311: 838-855. doi: <https://doi.org/10.1016/j.cma.2016.09.021>

29. Kim W, Reddy J. Novel explicit time integration schemes for efficient transient analyses of structural problems. *International Journal of Mechanical Sciences* 2020; 172: 105429. doi: <https://doi.org/10.1016/j.ijmecsci.2020.105429>
30. Belytschko T, Liu W, Moran B. *Nonlinear Finite Elements for Continua and Structures*. Nonlinear Finite Elements for Continua and Structures Wiley . 2000.
31. Talaslidis D, Wempner GA. The Linear Isoparametric Triangular Element - Theory And Application. *Computer Methods in Applied Mechanics and Engineering* 1993; 103(3): 375-397. doi: 10.1016/0045-7825(93)90129-1
32. Zienkiewicz OC, Taylor RL, Fox D. *The Finite Element Method for Solid and Structural Mechanics: Seventh Edition*. The Finite Element Method for Solid and Structural Mechanics: Seventh Edition . 2013
33. The Julia Project . The Julia Programming Language. <https://julialang.org/>; Accessed 03/13/2021.
34. Bezanson J, Edelman A, Karpinski S, Shah VB. Julia: A fresh approach to numerical computing. *SIAM review* 2017; 59(1): 65–98.
35. Petr Krysl . FinEtoolsFlexStructures: Finite Element tools for flexible beams and shells in Julia. <https://github.com/PetrKryslUCSD/FinEtoolsFlexStructures.jl>; Accessed 12/13/2021.
36. Bathe KJ, Ramm E, Wilson EL. Finite element formulations for large deformation dynamic analysis. *International Journal for Numerical Methods in Engineering* 1975; 9(2): 353-386. doi: <https://doi.org/10.1002/nme.1620090207>
37. Dassault Systèmes *Abaqus Theory Manual*. version 6.14 ed. 2014.
38. Tabiei A, Tanov R. A nonlinear higher order shear deformation shell element for dynamic explicit analysis: Part II. Performance validation through standard tests. *Finite Elements in Analysis and Design* 2000; 36(1): 39-50. doi: [https://doi.org/10.1016/S0168-874X\(00\)00006-8](https://doi.org/10.1016/S0168-874X(00)00006-8)
39. Oñate E, Cendoya P, Miquel J. Non-linear explicit dynamic analysis of shells using the BST rotation-free triangle. *Engineering Computations* 2002; 19(6): 662-706. doi: 10.1108/02644400210439119
40. Oñate E, Zárate F. Rotation-free triangular plate and shell elements. *International Journal for Numerical Methods in Engineering* 2000; 47(1-3): 557-603. doi: [https://doi.org/10.1002/\(SICI\)1097-0207\(20000110/30\)47:1/3<557::AID-NME784>3.0.CO;2-9](https://doi.org/10.1002/(SICI)1097-0207(20000110/30)47:1/3<557::AID-NME784>3.0.CO;2-9)

